ANALYSIS AND MODELING OF SHEAR WAVES GENERATED BY EXPLOSIONS AT THE SAN ANDREAS FAULT OBSERVATORY AT DEPTH

Justin L. Rubinstein, Fred F. Pollitz, and William L. Ellsworth

US Geological Survey

Sponsored by the National Nuclear Security Administration

Award No. DE-AI52-09NA29328
Proposal No. BAA09-69

ABSTRACT

Using multiple deployments of an 80-element, three-component borehole seismic array stretching from the surface to 2.3 km depth, we examine recordings of chemical explosions to better understand the generation of shear waves by explosive sources. The well is near vertical in the upper 1.5 km and gradually transitions to a dip of 38 degrees at the deepest recording location. The chemical shots are high-velocity chemical shots buried 3–4 m and fired electrically, ranging in size from 5 to 10 lb. The shotpoints are offset from the wellhead by approximately 40 m. Analysis of the recordings gives a velocity structure ranging from 1500 m/s in the upper 50 m to 5000 m/s at the bottom of the well. We also determine a Q structure using the spectral ratio method (e.g., Bath, 1974). Q(P) varies between 11 in the uppermost 50 m to 45 between 1000 m and 2350 m depth. The recordings have a strong, impulsive P arrival on the vertical channels. Additional, coherent phases arrive later on the vertical channel propagating at the P velocity. At the very near surface, there is evidence for a weak S arrival on the horizontal channels. We also observe S in the form of P to S conversions at layer boundaries further downhole.

We compute synthetic waveforms using the Direct Radial Integration method of Friederich and Dalkolmo (1995), which handles a layered transversely isotropic medium with anelasticity. We use the one-dimensional structure determined from the observations described above. For a zero-offset, shallow-burial purely explosive source the synthetics yield a highly impulsive P in addition to a small S, agreeing with our observations that the S is weak at vertical incidence, strengthening as the incidence angle decreases. The weak, near-surface S is generated from the surface reflection and subsequent conversion of the explosion generated P. We are presently investigating the source characteristics of the chemical shots, testing whether the waveforms can be completely matched using a purely explosive source or if there is a significant compensated linear vector dipole (CLVD) or secondary deformation (e.g., cavity collapse, distributed secondary shear dislocations) as well. This should shed light on the source radiation generated by chemical explosions and the interaction of shallow explosive sources with the free surface. Preliminary analysis indicates that a purely explosive source augmented by secondary distributed vertical shear (equivalent to a second-order moment tensor) directly above the explosive source is necessary to match our observations.

OBJECTIVES

The principal objective of the work being undertaken is to better characterize and understand the generation of S waves from explosive sources. The amplitudes of S waves are commonly used as a discriminant between explosion- and earthquake-generated sources, in that explosion sources primarily produce P waves. Thus, characterizing how S waves may be generated by explosive sources is critical to improving explosion discrimination criteria. In this project, we focus on S waves generated in the very near source region (~40 m laterally and 2.5 km in depth).

RESEARCH ACCOMPLISHED

Methods for Computing Synthetic Seismograms

Synthetic seismograms are generated using the direct Green's function (DGF) method of Friederich and Dalkolmo (1995). This method synthesizes the seismic wavefield for a spherically layered structure of seismic velocities Vp and Vs, density ρ, and attenuation factors Qp and Qs in the l−ω domain, where l denotes spherical harmonic degree. It is the spherical equivalent of the frequency-wavenumber method employed for flat-layered structures (e.g., Zhu and Rivera, 2002). It has been validated against analytic solutions, including those for elastic wave propagation in a full space for both isotropic and shear sources (Equation 4.29 of Aki and Richards [1980]) and in a half-space, e.g., Lamb's problem (Kuhn, 1985), as well as the independent numerical solutions AXITRA (Bouchon, 1981) and f − k method (Zhu and Rivera, 2002).

The DGF method is applied to buried sources using a layered structure determined by the P arrival times of the shots (Figures 1 and 2). The Vs structure is based on the Vp structure and the Vp/Vs ratio determined by regional tomography (Zhang et al., 2009), and the density structure is based on empirical Vp − ρ relationships (Gardner et al., 1984; Brocher, 2006). The Qp structure is based on fitting the decay in P-wave amplitude as a function of downhole distance using forward waveform modeling; it is consistent with modeling of the *P*-wave pulse width as a function of propagation distance (Rubinstein et al., 2011). The Qs values are not estimated from the data but are chosen such that the quality factor for bulk modulus is twice that for shear modulus.

For a x − y − z coordinate system (where x, y, and z denote distance in the due east, north, and "up" directions, respectively) and a point source located at $\mathbf{r}_0 = (x_0, y_0, z_0)$, we consider a moment tensor density $\mathbf{M}(\mathbf{r})$ given by

$$\mathbf{M} = M_{\mathrm{expl}} \begin{pmatrix} 1 & 0 & 0 \\ 0 & 1 & 0 \\ 0 & 0 & 1 \end{pmatrix} H(t)\delta(\mathbf{r}, \mathbf{r}_0) - M_{\mathrm{impl}} \begin{pmatrix} 1 & 0 & 0 \\ 0 & 1 & 0 \\ 0 & 0 & 1 \end{pmatrix} H(t-\delta t_{\mathrm{impl}})\delta(\mathbf{r}, \mathbf{r}_0)$$
$$- M_{xxz} \begin{pmatrix} 0 & 0 & 1 \\ 0 & 0 & 0 \\ 1 & 0 & 0 \end{pmatrix} H(t)\partial_{x_0}\delta(\mathbf{r}, (x_0, y_0, z')) - M_{yyz} \begin{pmatrix} 0 & 0 & 0 \\ 0 & 0 & 1 \\ 0 & 1 & 0 \end{pmatrix} H(t)\partial_{y_0}\delta(\mathbf{r}, (x_0, y_0, z')) \quad (1)$$

where H(t) is the step function, $\delta(\mathbf{r},\mathbf{r}_0)$ is the Dirac delta function, M_{expl} and M_{impl} are the moments associated with explosion and implosion source components, respectively, δt_{impl} is the delay in the implosive component, and M_{xxz} and M_{yyz} represent second-order moment tensor components (Backus and Mulcahy, 1976), which we shall relate to a distribution of vertical shear in a volume above $\mathbf{r}_0$. The notation (x_0, y_0, z') for these components is used to emphasize that the effective point source may be taken at a depth z' different from that of the explosive component z_0. The representations of M_{xxz} and M_{yyz} in Equation 1 may be verified by evaluating Equation 5.1b of Backus and Mulcahy (1976). This involves multiplying Equation 1 by $(x_0 - x)$ or $(y_0 - y)$, integrating over a volume $dV = dx_0\, dy_0\, dz'$, and integrating by parts with respect to x_0 (for M_{xxz}) or y_0 (for M_{yyz}).

Simulation of Explosive Sources and Their Fit to Downhole Observations

Synthetic seismograms using an explosive source and corresponding to the various shots are shown by the black traces in Figure 1. For Shot 2, the explosive source moment used for the synthetics is M_{expl} = 1.1 × 1010 N m, and for Shot 3 and Shot 5 it is M_{expl} = 4.3 × 1010 N m. The inclination of the borehole is within 5° of vertical for the first 1700 m and is progressively steeper at greater depth, up to 55° at 2.3 km depth, with a dip towards the northeast. Thus, the axial-component velocity is dominated by vertical velocity in the upper 1200 m and includes a progressively greater northeastward component with greater depth. The theoretical seismic radiation field depends upon the shot and receiver depths and the horizontal offset between shots and receivers. These horizontal offsets are generally less than 100 m in the upper 1700 m but increase with greater depth up to about 850 m at 2.3 km.

In order to guide the interpretation of observed and synthetic record sections in the vertical direction, we construct record sections in the horizontal direction at the depths of receiver #30 and #60 (Figure 3, a and b, respectively). Prominent arrivals include direct P and pS but also multiple reflections between the free surface and the base of a low-velocity, near-surface layer. P travel times from the shallowest receivers indicate a steep velocity gradient in the upper 100 m, Vp increasing from ~1.5 km/s at the surface to 2.6 km/s at 100 m. This is represented with two layers in the upper 100 m (Figure 2), the uppermost 50 m being of very low velocity (Figure 3 inset). Because the model discontinuity at 50 m is very sharp, P-wave reverberations are generated between the surface and this depth. The reverberations generated between the surface and this depth are labelled P_{mult}. The two-way travel time is 100 m/1.5 km/s = 0.067 sec. This is the difference in travel time between the direct P and successive reverberations that follow it (Figure 3).

Simulation of Non-Explosive Sources and Their Fit to Downhole Observations

Inference of non-explosive source components is based on a grid search for optimal values of source parameters (some subset of M_{impl} plus δt_{impl}, M_{xxz}, and M_{yyz}, corresponding to the second, third, and fourth terms of Equation 1) in which the root-mean-square misfit between observed and synthetic waveforms is minimized. For this purpose, a time window of length 0.15 sec starting just before the *P*-arrival is used to calculate the squared misfit, which is then summed over all contributing records and averaged. The secondary source components are assumed to be impulsive. Both direct P and P_{mult} are unambiguously observed at all depths between that of receiver #10 (depth = 183 m) for Shot 2 and receiver #200 for Shot 5 (Figure 1b,c,d), and they are replicated by the synthetics. In records #1–#3 recording Shot 2 (Figure 1a), the most prominent arrival in the synthetic seismograms is pS, which follows direct P by about 0.06 sec; their relatively large amplitude is due to the horizontal shot-receiver offset of ~40 m, which is a large fraction of the receiver depth (61.9, and 77.1 m for records #2–#3). The lack of such an arrival in the observed seismograms is an important clue to the source process. The addition of an implosion source (e.g., M_{impl} term of Equation 1) with modest delays δt_{impl} modifies synthetic waveforms only in the time interval between P and pS. Possible secondary source components that could augment the isotropic moment tensor components include point sources of shear (including CLVD components) or distributed shear.

We find that a model of distributed secondary vertical shear—on vertical planes close to the source depth—best replicates the observed seismograms. Our preferred model involves a distribution of vertical shear on vertical planes that comprise a cylinder of diameter Δx, laterally centered on the position of Shot 2, and placed at a nominal depth of 1.5 m. The moment tensor density components on the cylinder are of the form Mnz = constant = −M′, where n denotes the direction perpendicular to the surface of the cylinder towards its exterior. The secondary shear dislocations are collapsed onto the cylinder surface at depth 1.5 km so that they are distributed over a circle of circumference C = πΔx. Since Δx is small, it can be shown that this distribution is equivalent to the superposition of two second-order moment tensor components (Backus and Mulcahy, 1976) given by

$$M_{xxz} = M_{yyz} = -\frac{1}{4}(M'C)\,\Delta x \qquad (2)$$

We calculate the corresponding synthetics using the first, third, and fourth source terms of Equation 1, which for fixed M_{expl} depends upon M_{xxz} and M_{yyz}, which are equal, according to Equation 2. A grid search for optimal M_{xxz} is done using receivers #2 through #9 of Shot 2. This results in values $M_{xxz} = M_{yyz} = -(1.72\text{ m}) \times M_{expl}$ (Figure 4),

where M_{expl} = 1.1 × 1010 N m for Shot 2 (section 4). The resulting superposition of the isotropic moment tensor and higher-order moment tensor components for the shallow recordings of Shot 2 are shown in Figure 5. This model of combined isotropic first-order moment tensor and shear-type second-order moment tensor reduces the amount of shear-wave energy arising from the near surface, i.e., the explosion-generated pS and implosion-generated S (labelled pS+S(impl) in Figure 5a) destructively interfere. This model fits the shallowest Shot 2 recordings better than the model of isotropic source alone (Figure 1). The fits to recordings at greater depth (e.g., Shot 2 seismograms at the depth of receiver #10 and greater in Figure 5b) are found to be negligibly changed by the addition of the second-order moment tensor components.

For Shots 3 and 5, energy arriving 0.02–0.03 sec after direct P and of opposite polarity is best explained as the result of an implosive source acting with a small time delay after the initial chemical shot. We calculate the corresponding synthetics using the first and second source terms of Equation 1, with M_{impl} and δt_{impl} determined through a grid search. For Shot 3, receivers #90, #100, #110, #120, #130, #140, #150, and #159 are used; for Shot 5 only receivers #170, #180, #190, and #200 are used because the coherence between observed and synthetic records is poor for recordings at the deeper receivers. This analysis yields optimal $M_{impl} = 0.43 \times M_{expl}$ and $\delta t_{impl} = 0.027$ sec for Shot 3 (Figure 6a) and $M_{impl} = 0.34 \times M_{expl}$ and $\delta t_{impl} = 0.027$ sec for Shot 5 (Figure 6b). The resulting synthetics are shown in Figure 7a,b**.** The implosion-generated P (labelled P(impl) in Figure 7a for Shot 3) partially interferes with the explosion-generated P (labelled P). The improvement in fit over the corresponding synthetics for a purely isotropic source (Figure 1c,d) comes mainly from the M_{zz} component of the implosive source. Because of the high attenuation of S waves to depth ≥1 km from near-surface sources, Shot 3 and Shot 5 synthetics are nearly insensitive to possible CLVD components in either the explosive or implosive parts of the source.

Discussion

Trials of alternative models aimed at explaining particularly the character of the shallow Shot 2 recordings of Figure 1a were conducted using additional shear components of a first-order moment tensor, i.e.,

$$\mathbf{M} = M_{\text{expl}} \begin{pmatrix} 1 & 0 & 0 \\ 0 & 1 & 0 \\ 0 & 0 & 1 \end{pmatrix} H(t)\delta(\mathbf{r}, \mathbf{r}_0) + \begin{pmatrix} 0 & M_{xy} & M_{xz} \\ M_{xy} & 0 & M_{yz} \\ M_{xz} & M_{yz} & 0 \end{pmatrix} H(t)\delta(\mathbf{r}, \mathbf{r}_0) \tag{3}$$

These trials indicate that models involving the addition of a point vertical shear dislocation on any vertical plane, i.e., a non-zero M_{xz} or M_{yz} component in addition to the M_{expl} component), fail to explain the absence of energy traveling with the S wavespeed in the Shot 2 recordings. This is demonstrated in Figure 8, where parts (a) and (b) add additional trial M_{xz} components of opposite signs, and parts (c) and (d) similarly add additional trial M_{yz} components.

A stronger alternative model to explain the shallow Shot 2 recordings involves horizontal shear on a vertical plane, i.e., an M_{xy} component, in addition to the M_{expl} component of the chemical shot (Equation 3). A grid search for optimal M_{xy} yields $M_{xy} = 0.20 \times M_{expl}$ (Figure 9); the resulting misfit is smaller than that obtained for the second-order moment tensor model (Figure 4). This model fits the observed seismograms remarkably well (Figure 10). It would require strong horizontal shear stresses to be generated by the chemical explosion, causing failure of the surrounding rock. It would be plausible if there were strong asymmetry in the M_{xx} and M_{yy} components of the chemical shot, leading to strong horizontal shear at the source depth, or if lateral variations in material properties led to a similar concentration of horizontal shear. Hole-transverse component seismograms provide an additional means of comparing the second-order moment tensor and horizontal-shear models of secondary sources. The amplitude of motion transverse to the borehole (which is practically horizontal for the shallowest recordings of Shot 2), determined from the three-component seismograms, is the plotted quantity; phase information is not available because the non-axial recorded components are of uncertain orientation. The horizontal shear model exhibits more energy traveling at the S wavespeed (arriving at ≈ 0.09 sec and 0.10 sec for receivers #2 and #3, respectively) than the second-order moment tensor model. Although the observed seismograms are noisy, comparatively little energy is observed traveling at the S wavespeed, which favors the model of the second-order moment tensor.

Physically, the preferred secondary source components for Shot 2 represent uplift of a cylindrical volume of material directly above the explosion relative to the surrounding rock. The precise distribution of the additional inferred shear dislocations cannot be resolved, but the proposed mechanism is similar to that of damage of an inverted conical region above the explosion as proposed by Mosse (1981), i.e., block motion accommodated by near-vertical shear along the walls of the conical region. Our model could be refined by quantitative consideration of the vertical shear stress generated by the explosive source in order to localize those planes likely to undergo secondary shear failure. Sammis (2002) has proposed a more detailed model in which crack growth around the fault weakens the surrounding rock by decreasing its shear modulus, and secondary cracking according to his micro-mechanical model leads to additional source components. A non-dimensional interpretation of our results suggests that the second-order moment tensor source components scale with first-order moment tensor components with the ratio ~0.4 times the depth of burial of the explosion.

The implosive components inferred for Shots 3 and 5 represent collapse of a void temporarily created by the explosion. Its moment M_{impl} relative to the explosion moment M_{expl} is likely related to the amount of local rock failure induced by the explosion. In the absence of rock damage or fracturing, the explosion should not produce a permanent volume change, i.e., an implosion of net moment equal and opposite to the explosion is expected to follow the explosion. The fact that the ratio M_{impl}/M_{expl} is only a fraction of unity (values of 0.34 and 0.43 for Shot 3 and Shot 5, respectively) suggests a permanent macroscopic positive volume change and is in agreement with positive static moment inferred by Patton et al. (2005) for a series of chemical shots (1997 Kazakhstan depth-of-burial experiment) of much greater yield and depth of burial than those studied here.

CONCLUSIONS AND RECOMMENDATIONS

Downhole recordings of near-surface chemical explosions near the SAFOD Main Hole richly document the seismic wavefield at distances from ~70–2300 m from the source. Waveform modeling of these shots reveals that for smaller explosions the effective source may be described, to first order, as the superposition of an explosive point source and secondary sources representing a distribution of vertical shear dislocations. For larger explosions, an additional implosive component, slightly delayed from the initial explosive source, is required. The nature of the secondary source components is likely more complicated than that presented here, but our modeling suggests that they accommodate failure of a weak upper crustal rock in response to large local shear and isotropic stresses imparted by the chemical explosion. Continuing work will focus on analyzing data from more source-receiver pairs that are more distant. In particular, we will examine shots 10–20 km from a downhole array of instruments to analyze the generation of shear waves in the near field instead of the very near field.

ACKNOWLEDGEMENTS

Data has been provided by Paulsson Geophysical Services Inc. SAFOD is a part of Earthscope, a program funded by the National Science Foundation and carried out in cooperation with the U.S. Geological Survey, the International Continental Scientific Drilling Program, Stanford University, NASA, and other agencies. We thank Joe Fletcher and Paul Spudich for their comments on a preliminary draft.

REFERENCES

Aki, K. and P. G. Richards (1980). *Quantitative Seismology*, Vol. 1., W. H. Freeman and Company, San Francisco.

Backus, G. and M. Mulcahy (1976). Moment tensors and other phenomenological descriptions of seismic source, Part I. Continuous displacements, *Geophys. J. Roy. Astr. Soc*. 46: 341–361.

Bath, M. (1974). Spectral analysis in geophysics, in *Developments in Solid Earth Geophysics*, Elsevier, Amsterdam.

Bouchon, M. (1981). A simple method to calculate greens functions for elastic layered media. *Bull. Seismol. Soc. Am*. 71: 959–971.

Brocher, T. M. (2006). Empirical relations between elastic wavespeeds and density in the Earth's crust, *Bull. Seismol. Soc. Am.* 95: 2081–2092.

Friederich, W. and J. Dalkolmo (1995). Complete synthetic seismograms for a spherically symmetric earth by a numerical computation of the greens function in the frequency domain, *Geophys. J. Int.* 122: 537–550.

Gardner, G. H. F., L. W. Gardner, and A. R. Gregory (1984). Formation velocity and density—The diagnostic basics for stratigraphic traps, *Geophys*. 39: 770–780.

Kuhn, M. J. (1985). A numerical study of Lamb's problem, *Geophys. Prospecting* 33: 1103–1137.

Mosse, R. P. (1981). Review of seismic source models for underground nuclear explosions, *Bull. Seismol. Soc. Am*. 71: 1249–1268.

Patton, H., J. L. Bonner, and I. N. Gupta (2005). Rg excitation by underground explosions: Insights from source modelling the 1997 Kazakhstan depth-of-burial experiment, *Geophys. J. Int.* 163: 1006–1024.

Rubinstein, J. L., F. F. Pollitz, and W. L. Ellsworth (2011). Analysis and modeling of the wavefield generated by explosions at the San Andreas Fault Observatory at depth, *Seismol. Res. Lett.* 82: 272.

Sammis, C. G. (2002). Generation of high-frequency P and S wave energy by rock fracture during a buried explosion: Its effect on P/S discriminants at low magnitude, in *Proceedings of the 24th Seismic Research review—Nuclear Explosion Monitoring: Innovation and Integration*, LA-UR-02-5048, Vol. I, pp. 542–551.

Zhang, H., C. Thurber, and P. Bedrosian (2009). Joint inversion for Vp, Vs, and Vp/Vs at SAFOD, Parkfield, California, *Geochem. Geophys. Geosyst.* 10:Q11002, doi:10.1029/2009GC002709.

Zhu, L. and L. A. Rivera (2002). A note on the dynamic and static displacements from a point source in multilayered media, *Geophys. J. Int*. 148: 619–627.

Table 1. Details of small-offset shots from SAFOD wellhead

Shot Number	Date	Time (UTC) Hh:mm:ss	# Holes (10 ft deep)	Shot Size (lb)	Northing Offset (feet)	Easting Offset (feet)
2	4/28/2005	21:25:00	1	7	97.5	89.1
3	4/29/2005	15:05:00	2 (@ 5 lb)	10	112	65.4
5	4/29/2005	20:28:00	2 (@ 5 lb)	10	103.9	77.7

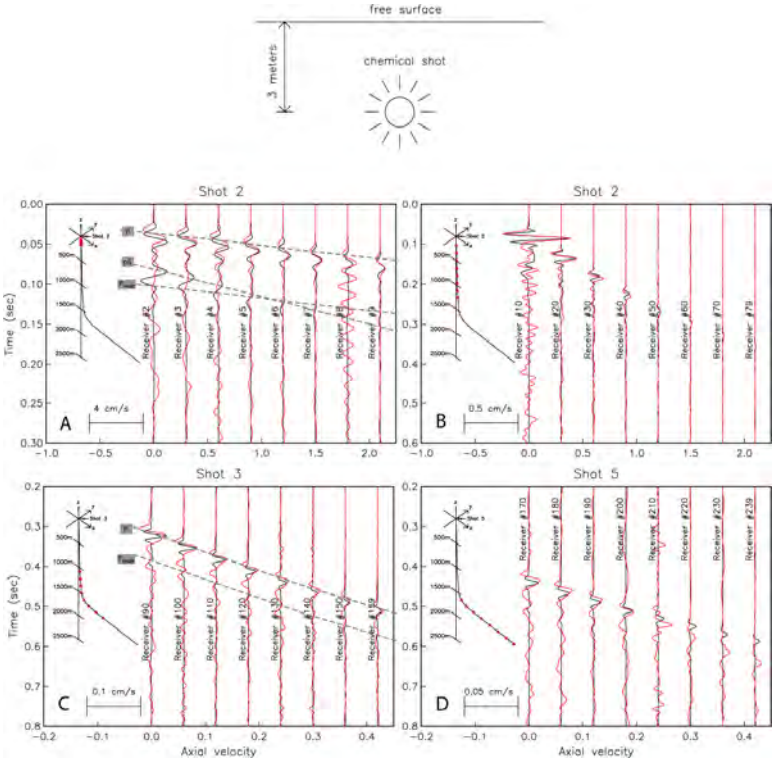

Figure 1. Observed axial-component seismograms (red) and synthetic seismograms (black) for each of the three shots recorded by downhole receiver arrays (Table 1). Parts (a) through (d) show different shots and/or groups of receivers. Both observed and synthetic traces have been deconvolved to velocity using an acausal filter generated by a cosine taper in the frequency domain between $\omega c = 2\pi/Tc$ and $2\omega c$, where Tc is a corner period chosen to be 0.023 sec; the corresponding corner frequency is $\omega c/2\pi = 43.5$ Hz. All traces are true amplitude, i.e., identical scaling of individual traces for each shot. The inset shows the positions of the seismometers corresponding to the plotted traces (small red triangles) in the SAFOD Main Hole. Only the explosion component M_{expl} is used to generate these synthetics; other source components of Equation 1 (M_{impl}, M_{xxz}, and M_{yyz}) are zero. Selected seismic phases are indicated with dashed gray lines.

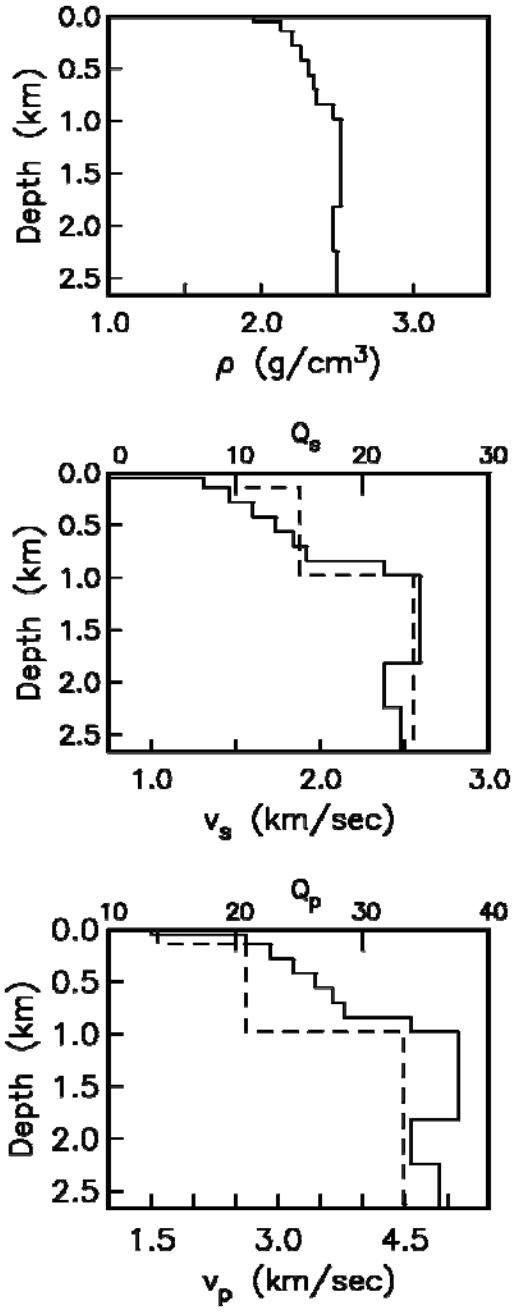

Figure 2. Layered structure of P and S velocities Vp and Vs, density ρ, and P- and S-wave quality factors Qp and Qs (dashed lines) as a function of depth.

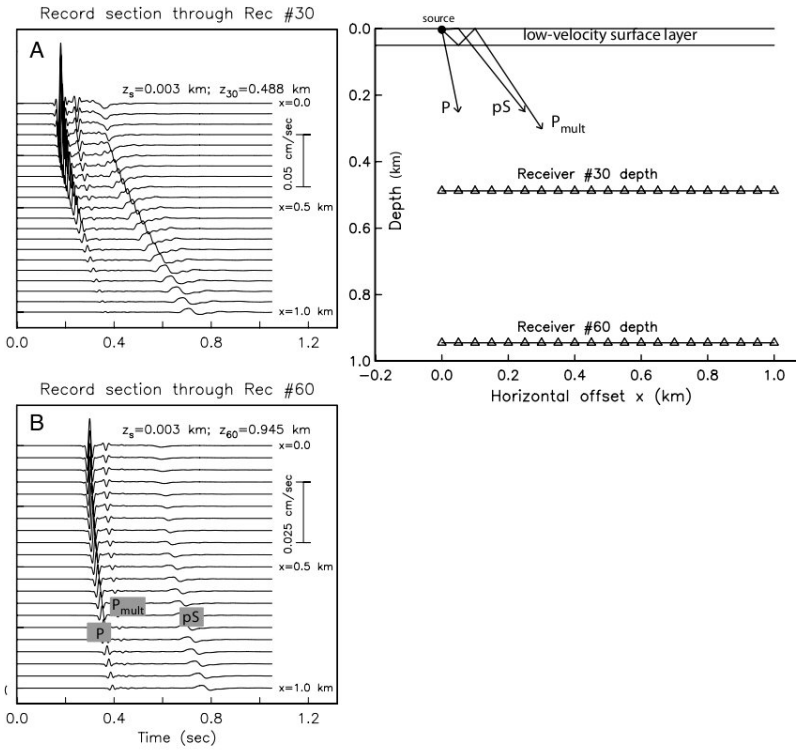

Figure 3. Vertical-component velocity seismograms as a function of lateral distance x from an isotropic source buried 3 m. (a) Array at depth of receiver #30 (0.4884 km). (b) Array at depth of receiver #60 (0.9455 km). The inset indicates the geometry of direct P, pS, and multiple reflections between the free surface and the base of the low-velocity near-surface layer P_{mult}.

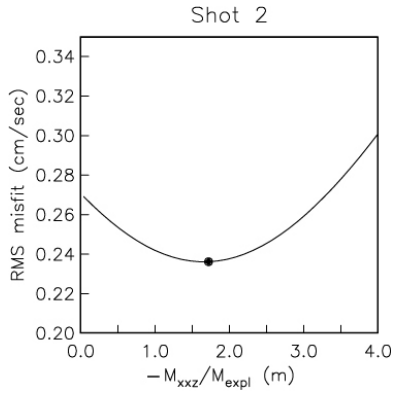

Figure 4. Root-mean-square misfit between observed and synthetic seismograms for Shot 2 computed using 0.15-sec-long portions of the contributing seismograms beginning just before the P arrival. The synthetics are calculated using the first, third, and fourth source terms of Equation 1; the third and fourth terms are parameterized with second-order moment tensor components M_{xxz} and M_{yyz}, which are equal (Equation 2). Optimal $M_{xxz} = M_{yyz} = -$ (1.72 m) $\times M_{expl}$ is indicated with the solid circle.

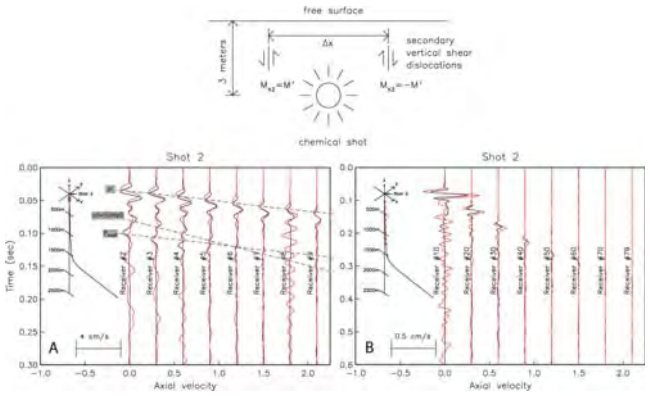

Figure 5. Observed axial-component seismograms (red) and synthetic seismograms (black) for Shot 2 (Table 1). Parts (a) and (b) show Shot 2 results for different groups of receivers. Synthetics are calculated using the combined explosion source and higher-order moment tensor model. The inset indicates the geometry of moment tensor density on the edge of a cylinder of diameter Δx used to represent secondary shear dislocations. Selected seismic phases are indicated with dashed gray lines. The designation pS+S(impl) denotes the combination of explosion-generated pS and implosion-generated S. Other details as in Figure 1.

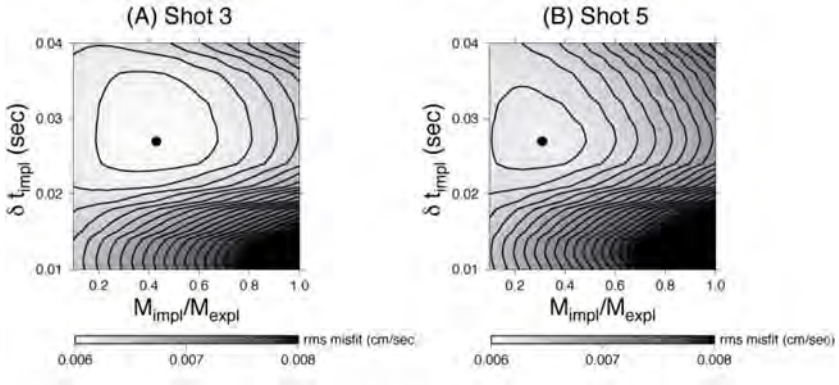

Figure 6. Root-mean-square misfit between observed and synthetic seismograms computed using 0.15-sec-long portions of the contributing seismograms beginning just before the P arrival. The synthetics are calculated using the first two source terms of Equation 1; the second term is parameterized with implosive moment M_{impl} and time delay δt_{impl}. (a) Shot 3, with optimal $M_{impl} = 0.43 \times M_{expl}$ and $\delta t_{impl} = 0.027$ sec (solid circle). (b) Shot 5, with optimal $M_{impl} = 0.34 \times M_{expl}$ and $\delta t_{impl} = 0.027$ sec (solid circle).

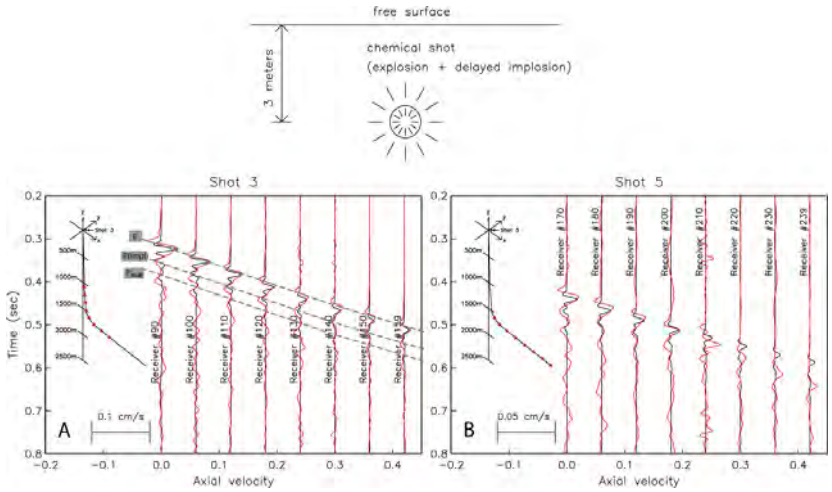

Figure 7. Observed axial-component seismograms (red) and synthetic seismograms (black) for (a) Shot 3 and (b) Shot 5 (Table 1). For Shots 3 and 5, the synthetics are calculated using the combined explosion source and delayed implosion model. Selected seismic phases are indicated with dashed gray lines. The designation P(impl) denotes the implosion-generated P. Other details as in Figure 1.

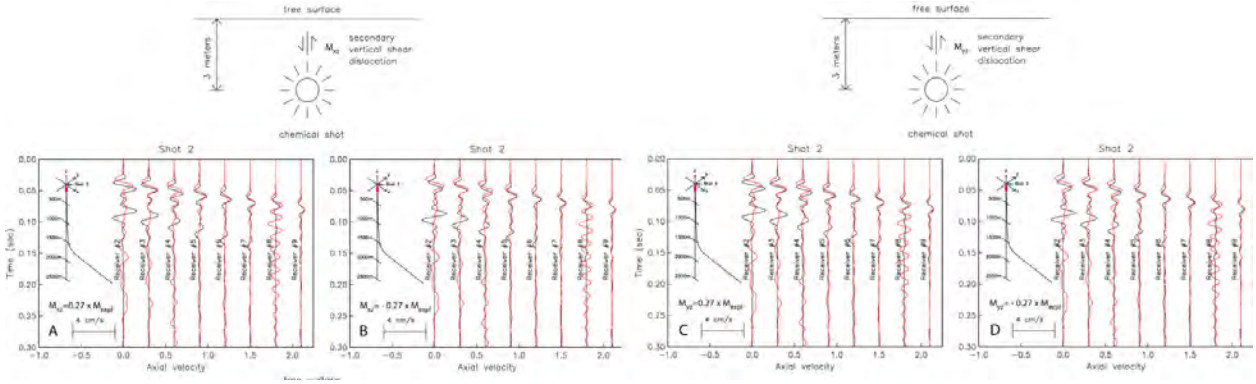

Figure 8. Observed axial-component seismograms (red) and synthetic seismograms (black) for receivers #2–#9 recording Shot 2 (Table 1). Parts (a) through (d) show the identical observed seismograms superimposed with synthetics generated with different secondary source components. Synthetics are calculated using a combined explosion source and secondary moment tensor components M_{xz} and M_{yz} with vertical shear (Equation 3). The inset indicates the geometry of moment tensor density at depth 1.5 m, directly above the explosion source used to represent secondary shear dislocations. Other details as in Figure 1.

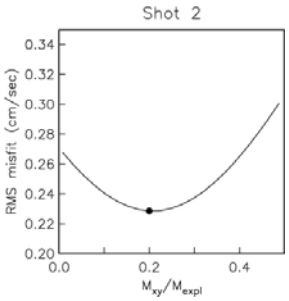

Figure 9. Root-mean-square misfit between observed and synthetic seismograms for Shot 2 computed using 0.15-sec-long portions of the contributing seismograms beginning just before the P arrival. The synthetics are calculated using the M_{expl} and M_{xy} source terms of Equation 3. Optimal $M_{xy} = 0.20 \times M_{expl}$ is indicated with the solid circle.

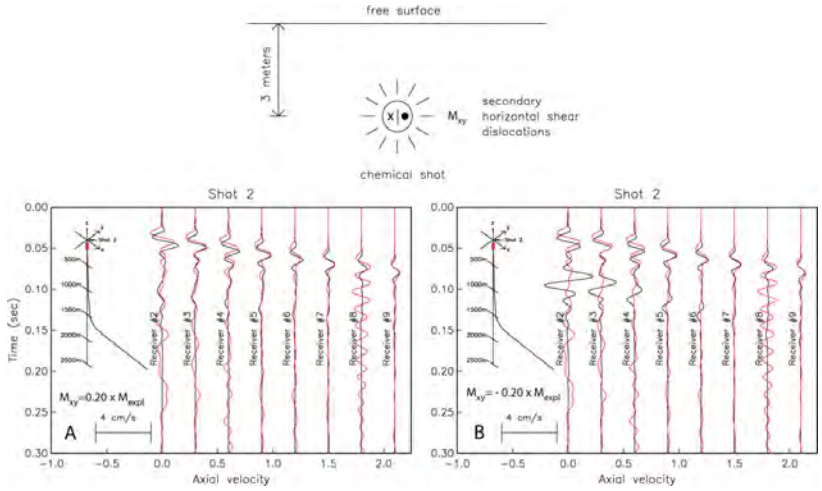

Figure 10. Observed axial-component seismograms (red) and synthetic seismograms (black) for receivers #2–#9 recording Shot 2 (Table 1). Synthetics are calculated using a combined explosion source and an additional moment tensor M_{xy} component with horizontal shear (Equation 3). The inset indicates the geometry of moment tensor density, placed at the same location as the explosion source, used to represent the secondary shear dislocation. Other details as in Figure 1.